

Differential gain, differential index, and linewidth enhancement factor for a 4 μm superlattice laser active layer

S. A. Anson,^{a)} J. T. Olesberg, Michael E. Flatté, T. C. Hasenberg, and Thomas F. Boggess^{a),b)}

Department of Physics and Astronomy, Optical Science and Technology Center, University of Iowa, Iowa City, Iowa 52242

(Received 11 January 1999; accepted for publication 8 April 1999)

We describe temporally and spectrally resolved measurements of the material differential gain, differential refractive index, and linewidth enhancement factor for a multilayer superlattice intended for use in midwave-infrared semiconductor lasers. We find good agreement between measured quantities and theoretical predictions based on a superlattice $\mathbf{K}\cdot\mathbf{p}$ formalism. The superlattice was designed for suppression of Auger recombination and intersubband absorption, and we find that the strategies employed in this process result in other characteristics that are desirable in a semiconductor laser gain medium. Specifically, for carrier densities and wavelengths appropriate to threshold in an optimized cavity configuration, this structure has a differential gain of approximately $1.5 \times 10^{-15} \text{ cm}^2$, a value comparable to that reported for near-infrared strained quantum wells. The peak gain and peak differential gain are nearly spectrally coincident, leading to a small value for the differential index. The large differential gain and small differential index result in a linewidth enhancement factor of less than one. This indicates that filamentation in high-power lasers based on this superlattice should be suppressed and that this structure is attractive for use in midwave-infrared lasers designed for spectrally pure operation. © 1999 American Institute of Physics.

[S0021-8979(99)02114-3]

I. INTRODUCTION

Midwave-infrared (MWIR, 2–5 μm) diode and optically pumped semiconductor lasers¹ have significant potential applications in the areas of remote sensing, medical diagnostics, and infrared countermeasures. This has driven intense research efforts focused on these devices, which have led to continuing improvements in MWIR laser performance. Still these lasers remain an immature technology, and demands on performance will continue to rise as attempts are made to implement these devices in practical optical systems.

To date, much of the emphasis on improved operation of *interband* MWIR lasers has focused on the achievement of room-temperature, continuous-wave operation through the suppression of Auger recombination and intersubband absorption (ISBA).² A significant subset of this work has been directed toward electronic structure engineering in type-II InAs/GalnSb superlattices and related structures.^{3–5} While this effort has met with some success, other fundamental properties of these laser materials, such as the differential gain and differential refractive index, have received considerably less attention. These parameters relate to another important fundamental laser property, the linewidth enhancement factor,

$$\alpha_{\text{lw}} = \frac{-4\pi}{\lambda} \frac{dn/dN}{d\gamma/dN}, \quad (1)$$

^{a)}Also with: Department of Electrical & Computer Engineering, University of Iowa.

^{b)}Electronic mail: thomas-boggess@uiowa.edu

a parameter that indicates the susceptibility of high-power lasers to filamentation and limits the spectral purity of single-mode lasers. In Eq. (1), n is the refractive index, γ is the material gain, N is the carrier density, and λ is the free-space wavelength. Filamentation, which is a result of self-focusing arising from a combination of gain saturation and the density-dependent refractive index, is substantially reduced in structures with linewidth enhancement factors less than 0.4.⁶ Since filamentation may result in poor beam quality, poor utilization of the available gain, and facet damage, reduction or elimination of this effect is highly desirable in high-power lasers. A small linewidth enhancement factor is also favorable for spectrally pure laser operation, since the linewidth of a single-mode semiconductor laser is⁷

$$\Delta\nu = \Delta\nu_{\text{ST}}(1 + \alpha_{\text{lw}}^2), \quad (2)$$

where $\Delta\nu_{\text{ST}}$ is the Schawlow–Townes linewidth. Since a variety of potential MWIR diode laser applications could benefit from spectrally pure operation, a small α_{lw} is highly beneficial.

Several methods exist for measuring the linewidth enhancement factor of a laser. This can be achieved, e.g., by using the small signal modulation technique⁸ or by measuring the net mode gain using the Hakki–Paoli technique and the density dependence of the index from the emission wavelength shift with injection current.⁹ The method used here is similar to that used by Henry and co-workers.¹⁰ Their technique relies on the extraction of the gain and absorption spectra from measurements of spontaneous emission spectra supplemented by measurements of the laser line energy and the differential quantum efficiency to determine the carrier

density. A Kramers–Kronig transformation is then used to extract the density dependence of the real part of the refractive index, thus leading to the linewidth enhancement factor. Here, we obtain the differential gain spectra for known carrier densities directly from time-resolved differential transmission measurements.

In this article, we describe measurements and calculations of the differential gain, differential refractive index, and the linewidth enhancement factor in a type-II, InAs/GaInSb-based superlattice designed as the active region of a MWIR laser. The structure is specifically configured for suppressed Auger recombination.¹¹ The strategies that result in small Auger rates and weak intersubband absorption at the band edge involve the use of electronic structure engineering: (1) to balance the conduction and valence band edge density of states through strain and quantum confinement (a strategy similar to that used for near-infrared (IR) semiconductors)¹² and (2) to arrange superlattice mini-gaps to eliminate final states for Auger and intersubband transitions. These same strategies result in a large differential gain $d\gamma/dN$, and therefore a small linewidth enhancement factor. In addition, for carrier densities appropriate to laser operation, the peak of the gain is spectrally located near the peak differential gain. This tends to minimize the differential refractive index dn/dN at the anticipated lasing wavelength, thereby also reducing the linewidth enhancement factor. We demonstrate a material linewidth enhancement factor of less than one in the MWIR structure discussed here. This may be compared to values of 2–5 that are typical of strained near-IR multiple-quantum-well lasers.

II. DETAILS OF THE SUPERLATTICE

The sample was grown by molecular beam epitaxy (MBE) on a nominally undoped GaSb substrate and consists of (in order of growth) a 3000 Å GaSb buffer layer, a 1000 Å $\text{Al}_{0.30}\text{Ga}_{0.42}\text{In}_{0.28}\text{As}_{0.27}\text{Sb}_{0.73}$ carrier-confinement layer, 40 periods of a 4-layer superlattice, another 1000 Å $\text{Al}_{0.30}\text{Ga}_{0.42}\text{In}_{0.28}\text{As}_{0.27}\text{Sb}_{0.73}$ carrier-confinement layer, and a 100 Å GaSb cap. A single period of the superlattice, which is shown schematically in Fig. 1(a), is comprised of 16.5 Å of InAs, 25.9 Å of $\text{Ga}_{0.65}\text{In}_{0.35}\text{Sb}$, 16.5 Å of InAs, and 38.7 Å of $\text{Al}_{0.27}\text{Ga}_{0.48}\text{In}_{0.25}\text{As}_{0.43}\text{Sb}_{0.57}$. The room-temperature photoluminescence for this structure is peaked at 3.84 μm . Fitting of the photoluminescence spectrum yields a room-temperature band gap of approximately 4 μm . The structural properties of the superlattice (alloy compositions and layer thicknesses) were determined using a self-consistent analysis of the photoluminescence spectrum, x-ray diffraction, and the MBE fluxes.

Through variations in only the layer thickness, the band-gap energy of this superlattice can be varied widely. Superlattices similar to that described here have been incorporated into diode lasers operating at 2.7 μm and optically pumped lasers operating at 3.7 μm up to room temperature and at 5.2 μm at temperatures up to 185 K.¹³ These structures are similar to the optically pumped “W lasers” studied by researchers at the Naval Research Laboratories and the University of Houston.^{5,14} In the present structure, however, the use of the

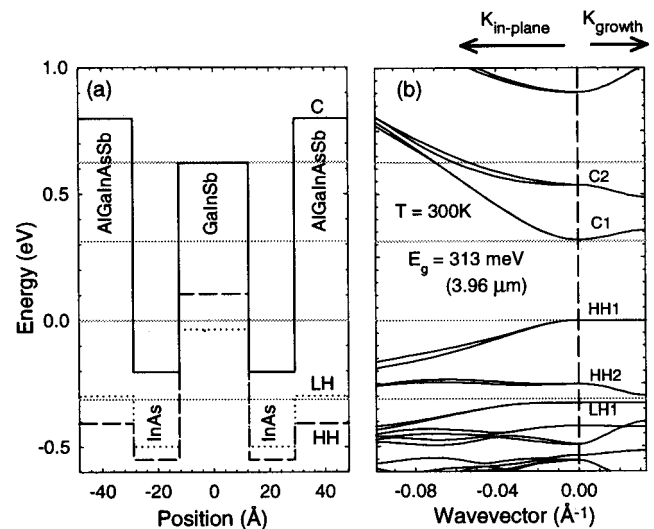


FIG. 1. (a) Conduction (solid), heavy-hole (dashed), and light-hole (dotted) band edges for one period of the four-layer superlattice. (b) eight-band superlattice $\mathbf{K}\cdot\mathbf{p}$ band structure for both the in-plane and growth directions. One band-gap energy below the valence band and one band-gap energy above the conduction band are indicated by the horizontal lines.

quinternary layers provides the potential for electrical carrier injection. In addition, it adds flexibility in the suppression of Auger recombination and intersubband absorption and for the engineering of the differential gain, differential index, and linewidth enhancement factor.

The band structure for this superlattice, shown in Fig. 1(b), was calculated using an eight-band superlattice $\mathbf{K}\cdot\mathbf{p}$ model that has been generalized to account for an arbitrary number of layers in a superlattice unit cell.³ Input parameters¹⁵ to the calculation are limited to energy levels, matrix elements, and effective masses of bulk constituents, and valence band offsets between layers. The recombination properties^{11,16} of this same four-layer superlattice and the optical properties of related type-II superlattice structures¹⁷ have been calculated using this superlattice $\mathbf{K}\cdot\mathbf{p}$ formalism and are found to be in excellent agreement with measured results. The four-layer superlattice was designed to have an isolated uppermost heavy-hole valence subband (HH1) with a light in-plane mass at the band edge ($m_{\text{HH1}} = 0.064m_0$) resulting in a disparity of only a factor of approximately 2 in the conduction and valence band-edge density of states. The next highest valence subband is more than 250 meV below HH1. These factors ensure that the electron and hole quasi-Fermi levels both move rapidly toward their respective band edges as carriers are injected, thereby leading to low transparency densities and high differential gain. In addition, an energy gap throughout the growth direction of the Brillouin zone was placed near one band-gap energy below the HH1 valence subband for the suppression of both hole Auger transitions and ISBA. This gap is evident in the theoretical ISBA spectra shown in Fig. 2(a). The theoretical gain spectra are shown in Fig. 2(b) for a comparison. We note that the suppression of ISBA is not optimized in this structure as it was designed specifically for the minimization of Auger recombination. Still, at carrier densities that would be typical of

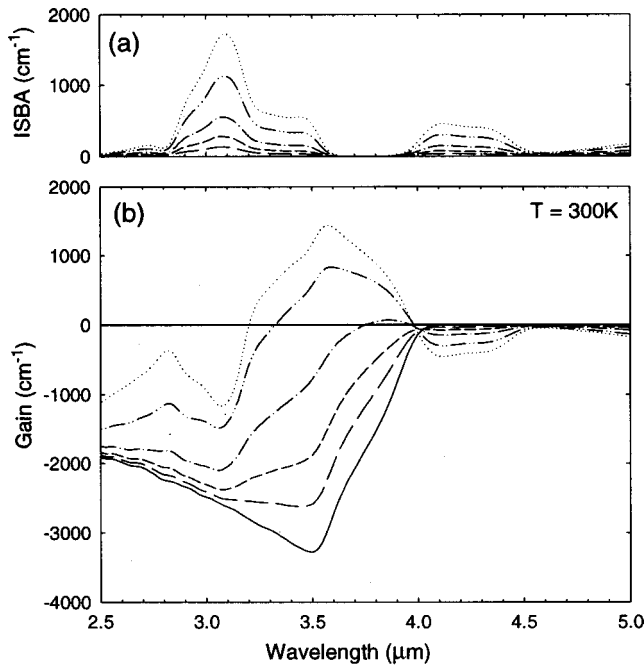


FIG. 2. (a) Intersubband absorption (ISBA) spectra and (b) gain spectra determined theoretically for the four-layer superlattice shown for the following carrier densities: 0 (solid), 1.3 (long dashed), 2.7 (short dashed), 5.3 (dash-dot), 10.6 (dash-dot-dot), and 15.9 (dotted) $\times 10^{17} \text{ cm}^{-3}$.

laser operation ($\sim 10^{18} \text{ cm}^{-3}$), the ISBA does not significantly reduce the peak gain for this structure.

III. EXPERIMENT

Time-resolved differential transmission was used to obtain spectra of the density-dependent change in absorption. The experimental configuration is similar to that described previously.^{17,18} Measurements were performed at room temperature using 140 fs pump pulses from a mode-locked Ti:sapphire laser operating at 843 nm and 170 fs probe pulses from a synchronously pumped optical parametric oscillator (OPO)¹⁹ tunable between 2.6 and 4.4 μm . The pump pulses were focused to a radius (e^{-1} of peak intensity) of 75 μm , and the probe pulses were focused on the center of the excited region of the sample with a radius of 32 μm . The pump and probe were separately chopped, and the transmitted probe was sent through a monochromator for added spectral resolution ($\sim 20 \text{ nm}$) and detected with a liquid-nitrogen-cooled InSb detector. The output of this detector was processed through a pair of parallel lock-in amplifiers separately tuned to the probe chopping frequency and the sum of the pump and probe chopping frequencies. The former allowed for corrections of long-term drift in the output power of the OPO, while the latter provided a signal proportional to the pump-induced change in the probe transmission.

The pump pulses generate a dense and initially very hot electron-hole population that is observed to cool to near lattice temperature within approximately 10 ps. On a much longer time scale the carriers recombine primarily by Auger and Shockley-Read-Hall recombination. By measuring the transmission of the probe as a function of time delay at a wavelength near the band edge, the evolution of the band edge population may be extracted. Such measurements

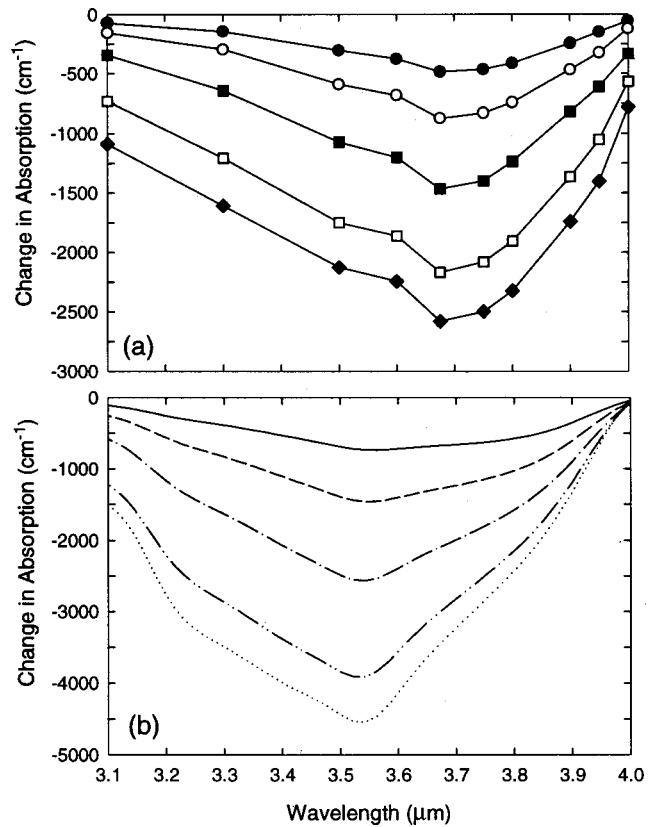


FIG. 3. (a) Experimental carrier-induced change in absorption spectra for the following carrier densities: 1.3 (filled circles), 2.7 (open circles), 5.3 (filled squares), 10.6 (open squares), and 15.9 (filled diamonds) $\times 10^{17} \text{ cm}^{-3}$ and (b) theoretical carrier-induced change in absorption spectra for the following carrier densities: 1.3 (solid), 2.7 (dashed), 5.3 (dash-dot), 10.6 (dash-dot-dot), and 15.9 (dotted) $\times 10^{17} \text{ cm}^{-3}$.

readily provide the carrier recombination rate, which is described in detail for this structure elsewhere.^{11,16} Alternatively, the probe delay can be set longer than the carrier cooling time but shorter than the time required for recombination, and the transmission can be measured as a function of probe wavelength. This allows the probe transmission spectrum to be analyzed for a fixed and well-defined carrier density, and by varying the pump excitation level the density dependence of the transmission spectrum can be determined.

IV. RESULTS

The tunability of the OPO allows us to explore the density-dependent optical properties of the superlattice over a broad spectral range. In Fig. 3(a) we show the results of measurements of the change in absorption $\Delta\alpha$ as a function of probing wavelength in the range of 3.1–4.0 μm for carrier densities ranging from 1.3 to 15.9 $\times 10^{17} \text{ cm}^{-3}$. These results are obtained directly from the differential transmission data using

$$\Delta\alpha = \frac{-1}{L} \ln \left(1 + \frac{\Delta T}{T} \right), \quad (3)$$

where L is the superlattice thickness and $\Delta T/T$ is the fractional change in the probe transmission. The carrier density for these measurements has been calibrated by comparing

measured and calculated time-resolved photoluminescence spectra, as described elsewhere,¹⁶ and is consistent with the photon density in the pump pulses.

In Fig. 3(b) we show calculated spectra of $\Delta\alpha$ for the same set of carrier densities used to obtain the data in Fig. 3(a). The theoretical results were obtained using the calculated band structure and momentum-dependent matrix elements with no adjustable parameters. ISBA is also included, but many-body effects are ignored. We find good agreement between the measured and calculated spectral and density dependencies for $\Delta\alpha$. There are, however, notable minor discrepancies. Specifically a 12 meV mismatch exists between the measured and calculated peak $\Delta\alpha$, apparently as a consequence of a theoretical overestimation of the width of the first miniband, and the peak magnitudes of the theoretical and experimental results differ by a factor of 1.8. The origins of such deviations are not known with certainty, but may be a result of remaining uncertainties in individual layer thicknesses and alloy compositions for the structure, uncertainties in material parameters such as the band offsets (particularly those associated with the quinary layers), and/or interface roughness. Many-body effects could also contribute to discrepancies. For example, it is clear from Fig. 3 that the experimental high-density data display evidence of band-gap renormalization, which is not included in the theory. Still, the overall agreement between theory and experiment is quite reasonable, indicating that the theoretical results can be used with reasonable confidence for predicting the optical properties of these superlattices. This ability is extraordinarily valuable for engineering the electronic and optical properties of superlattices for high-performance lasers and other device applications. On the other hand, the experimental results provide a direct measure of the actual optical properties, including those associated with many-body effects.

The differential gain $d\gamma/dN$ can be extracted readily by first fitting smooth functions through the curves in Fig. 3 at various wavelengths to obtain the density dependence of $\Delta\alpha$ at each of these wavelengths and then using

$$\frac{d\gamma}{dN} = \frac{d(-\Delta\alpha)}{dN}. \quad (4)$$

The results are shown in Fig. 4. Near the optimal threshold density²⁰ of $1.06 \times 10^{18} \text{ cm}^{-3}$, the theoretical peak gain occurs near $3.58 \mu\text{m}$, where the differential gain is approximately $1.5 \times 10^{-15} \text{ cm}^2$. The value of the differential gain is quite high, comparable to values reported for strained quantum wells designed for near-IR lasers.^{21,22} Again, the relatively large differential gain arises primarily from the low valence band-edge effective mass and the resulting balance between the conduction and valence band density of states.

A second quantity required in determining the linewidth enhancement factor is the differential index dn/dN . This can also be extracted from the data of Fig. 3 through a Kramers–Kronig transformation, which provides spectra of the change in index Δn for the various carrier densities. The results of such a calculation for Δn are shown in Figs. 5(a) and 5(b) for the experimental and theoretical data, respectively. The experimental curve was arrived at by first fitting smooth curves through the data in Fig. 3 and then performing the

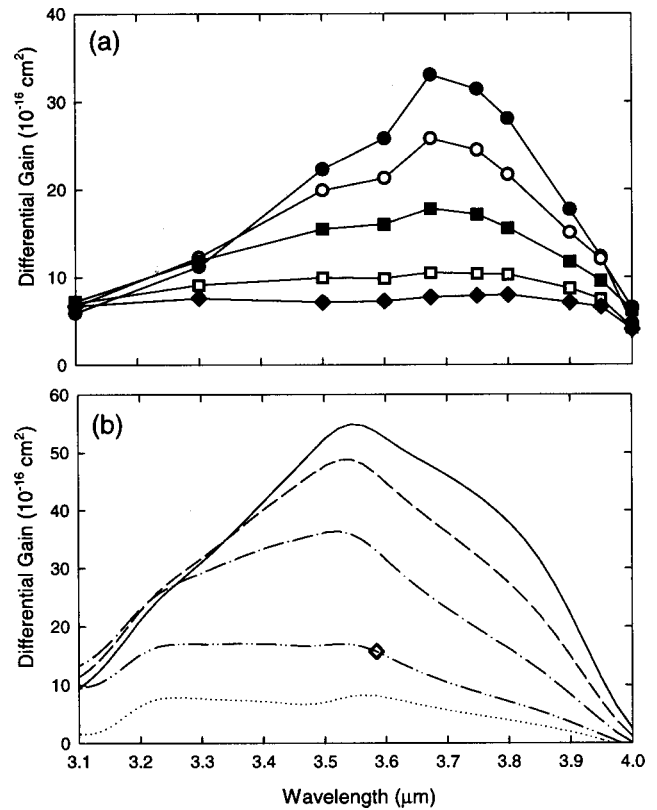


FIG. 4. (a) Experimental differential gain spectra for the following carrier densities: 1.3 (filled circles), 2.7 (open circles), 5.3 (filled squares), 10.6 (open squares), and 15.9 (filled diamonds) $\times 10^{17} \text{ cm}^{-3}$ and (b) theoretical differential gain spectra for the following carrier densities: 1.3 (solid), 2.7 (dashed), 5.3 (dash-dot), 10.6 (dash-dot-dot), and 15.9 (dotted) $\times 10^{17} \text{ cm}^{-3}$. The differential gain at the wavelength corresponding to the peak theoretical gain at threshold ($1.06 \times 10^{18} \text{ cm}^{-3}$) is indicated by the open diamond.

Kramers–Kronig transformation on the smoothed curves. Again, reasonable agreement between theory and experiment is observed, with the discrepancies being traced directly to the discrepancies in the $\Delta\alpha$ spectra. In particular, the magnitudes of the experimental and theoretical spectra of Δn agree well, but the zero crossings differ, primarily as a consequence of the differences in the spectral locations of the peaks in the theoretical and experimental spectra of $\Delta\alpha$.

The Kramers–Kronig transformations provide only estimates of the density dependent refractive index. That is, the Kramers–Kronig transformation requires an integration over *all* frequencies, yet the available data extend only from 3.1 to 4 μm . Hence, the impact of the limited spectral range of the $\Delta\alpha$ data must be carefully considered in evaluating Δn . To examine these effects, we have *calculated* the density-dependent absorption spectra over the range from 1.24 to 23.3 μm and have performed the Kramers–Kronig transformation of these spectra. This process, which leads to the spectra shown in Fig. 5(c), differs from that leading to the results in Fig. 5(b) in two important ways: (1) the range of integration in the Kramers–Kronig transformation is greatly extended in this case so that, within the range of the experimental data, the influence of the end points are less pronounced, and (2) the transformation includes spectral regions that exhibit strong intersubband absorption features not present in the more limited range used for Figs. 5(a) and

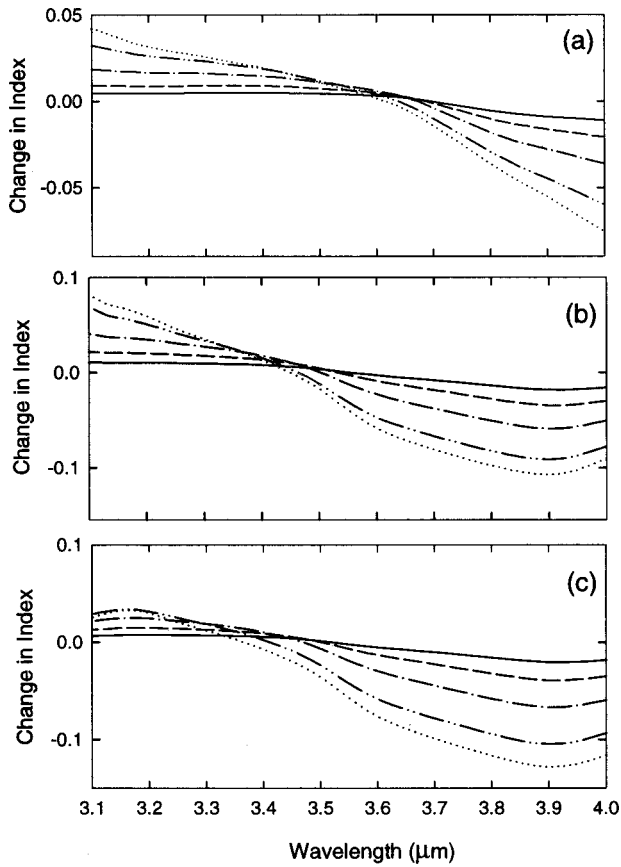


FIG. 5. Carrier-induced change in refractive index, for the carrier densities: 1.3 (solid), 2.7 (dashed), 5.3 (dash-dot), 10.6 (dash-dot-dot), and 15.9 (dotted) $\times 10^{17} \text{ cm}^{-3}$, obtain (a) by using the experimental $\Delta\alpha(N)$, (b) by truncating the theoretical $\Delta\alpha(N)$ to the experimental spectral range (3.1–4.0 μm), (c) by using the full theoretically determined $\Delta\alpha(N)$ from 1.24 to 23.3 μm (996–53.2 meV).

5(b). The relative importance of these two effects can be determined readily by simply neglecting ISBA in the theory. This process reveals that the differences in the spectra shown in Figs. 5(b) and 5(c) are primarily a consequence of the endpoints rather than the ISBA features. We emphasize, however, that the discrepancies between the experimental and theoretical index spectra are relatively minor in the region near the peak gain.

The results shown in Fig. 5 can be used to extract the theoretical and experimental differential index dn/dN , as shown in Fig. 6. Again, for the calculated threshold density of $1.06 \times 10^{18} \text{ cm}^{-3}$, the theoretical peak gain occurs near 3.58 μm , where the differential index is approximately $4 \times 10^{-20} \text{ cm}^3$. This value is slightly larger than the values of $(1-3) \times 10^{-20} \text{ cm}^3$ typical in near-IR lasers.^{21,23}

Once dn/dN and $d\gamma/dN$ are known, the linewidth enhancement factor α_{lw} can be determined from Eq. (1). The experimental and calculated spectra of α_{lw} are shown in Fig. 7. In both cases we find that, for carrier densities and wavelengths that would be appropriate to laser operation, the linewidth enhancement factor is less than one. This can be compared to typical values of 2–5 reported for near-IR strained quantum-well lasers.^{22–25}

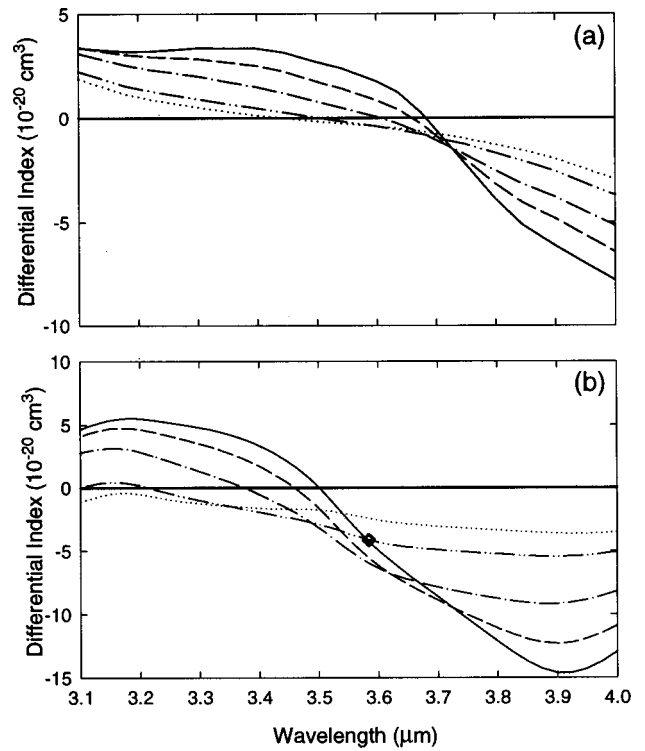


FIG. 6. The experimental (a) and theoretical (b) differential index for the carrier densities: 1.3 (solid), 2.7 (dashed), 5.3 (dash-dot), 10.6 (dash-dot-dot), and 15.9 (dotted) $\times 10^{17} \text{ cm}^{-3}$. The diamond indicates the predicted lasing wavelength at the optimal carrier density.

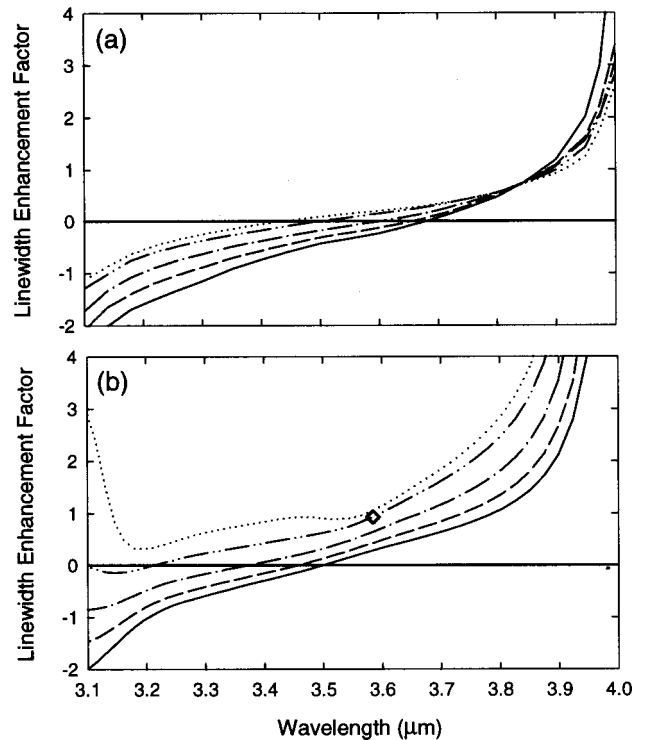


FIG. 7. The experimental (a) and theoretical (b) linewidth enhancement factors for the carrier densities: 1.3 (solid), 2.7 (dashed), 5.3 (dash-dot), 10.6 (dash-dot-dot), and 15.9 (dotted) $\times 10^{17} \text{ cm}^{-3}$. The linewidth enhancement factor and wavelength of the peak theoretical gain at threshold ($1.06 \times 10^{18} \text{ cm}^{-3}$) is indicated by the open diamond.

V. SUMMARY AND CONCLUSIONS

We have used time-resolved differential transmission to measure the carrier-induced change in absorption, differential gain, differential index, and the linewidth enhancement factor for a four-layer superlattice designed for use as an active region in mid-infrared semiconductor lasers. The structure has a differential material gain comparable to that measured in near-IR strained quantum-well lasers. We have found good agreement between measured results and calculations based on an eight-band superlattice $\mathbf{K}\cdot\mathbf{p}$ formalism. A Kramers–Kronig transformation of these results was used to evaluate the differential material refractive index, which is slightly larger than that measured in near-IR lasers. The large differential gain results in a small linewidth enhancement factor, which is less than one at wavelengths and carrier densities appropriate to laser operation. The small linewidth enhancement factor will reduce the effects of filamentation in high-power MWIR lasers and/or reduce the spectral linewidth in single-mode MWIR lasers incorporating this multilayer superlattice as the active region.

We emphasize that the parameters (differential gain and index, linewidth enhancement factors, etc.) extracted from these studies are purely material properties and that the impact of the optical cavity must be considered in an actual laser. Our approach focuses on the active region material itself, which for MWIR lasers is typically engineered for suppression of Auger recombination and intersubband absorption. The impact of this engineering on the differential gain and index and on the linewidth enhancement factor has, to this point, been largely overlooked. The technique employed here allows for a convenient means of screening engineered active regions for these important properties without the need for processing and fabricating working devices. This, when coupled with measurements of carrier recombination in the active regions, should lead to a complete picture of the suitability of the engineered material for use in high-performance MWIR lasers.

ACKNOWLEDGMENTS

This research was supported in part by the United States Air Force, Air Force Materiel Command, Air Force Research Laboratory, Kirtland AFB New Mexico 87117-5777 (Contract No. F29601-97-C-0041) and the National Science Foundation (Grant No. ECS-9707799).

¹See, e.g., R. H. Miles and T. C. Hasenberg, in *Antimonide Related Strain-Layer Heterostructures*, edited by M. O. Manasreh (Gordon and Breach, Amsterdam, 1998), pp. 433–460; J. I. Malin, C. L. Felix, J. R. Meyer, C. A. Hoffman, J. F. Pinto, C.-H. Lin, P. C. Chang, S. J. Murry, and S.-S.

Pei, *Electron. Lett.* **32**, 1593 (1996); K. D. Moiseev, M. P. Mikhailova, O. G. Ershov, and Yu. P. Yakovlev, *Fiz. Tekh. Poluprovodn.* **30**, 399 (1996) *Sov. Phys. Semicond.* **30**, 223 (1996); H. K. Choi, G. W. Turner, M. J. Manfra, and M. K. Conners, *Appl. Phys. Lett.* **68**, 2936 (1996); S. R. Kurtz, R. M. Biefeld, A. A. Allerman, A. J. Howard, M. H. Crawford, and M. W. Pelczynski, *ibid.* **68**, 1332 (1996); D. Z. Garbuzov, R. U. Martinielli, H. Lee, P. K. York, L. A. DiMarco, M. G. Harvey, R. J. Matarese, S. Y. Narayan, and J. C. Connolly, *ibid.* **70**, 2931 (1997), and references therein.

²For a recent review, see C. R. Pidgeon, C. M. Ciesla, and B. N. Murdin, *Prog. Quantum. Electron.* **21**, 361 (1998).

³M. E. Flatté, J. T. Olesberg, S. A. Anson, T. F. Boggess, T. C. Hasenberg, R. H. Miles, and C. H. Grein, *Appl. Phys. Lett.* **70**, 3212 (1997).

⁴M. E. Flatté, C. H. Grein, H. Ehrenreich, R. H. Miles, and H. Cruz, *J. Appl. Phys.* **78**, 4552 (1995); C. H. Grein, P. M. Young, and H. Ehrenreich, *ibid.* **76**, 1940 (1994).

⁵J. R. Meyer, C. A. Hoffman, F. J. Bartoli, and L. R. Ram-Mohan, *Appl. Phys. Lett.* **67**, 757 (1995).

⁶J. R. Marciantie and G. P. Agrawal, *Appl. Phys. Lett.* **69**, 593 (1996).

⁷C. H. Henry, *IEEE J. Quantum Electron.* **18**, 259 (1982).

⁸C. Harder, K. Vahala, and A. Yariv, *Appl. Phys. Lett.* **42**, 328 (1983).

⁹I. D. Henning and J. V. Collins, *Electron. Lett.* **19**, 927 (1983); B. W. Hakki and T. L. Paoli, *J. Appl. Phys.* **46**, 1299 (1975).

¹⁰C. H. Henry, R. A. Logan, and F. R. Merritt, *J. Appl. Phys.* **51**, 3042 (1980); C. H. Henry, *IEEE J. Quantum Electron.* **18**, 259 (1982).

¹¹M. E. Flatté, C. H. Grein, T. C. Hasenberg, S. A. Anson, D.-J. Jang, J. T. Olesberg, and T. F. Boggess, *Phys. Rev. B* **59**, 5745 (1999).

¹²E. Yablonovitch and E. O. Kane, *J. Lightwave Technol.* **6**, 1292 (1986); E. P. O'Reilly and A. R. Adams, *IEEE J. Quantum Electron.* **30**, 366 (1994).

¹³M. E. Flatté, T. C. Hasenberg, J. T. Olesberg, S. A. Anson, T. F. Boggess, C. Yan, and D. L. McDaniel, Jr., *Appl. Phys. Lett.* **71**, 3764 (1997).

¹⁴J. I. Malin, J. R. Meyers, C. L. Felix, J. R. Lindle, L. Goldberg, C. A. Hoffman, F. J. Bartoli, C.-H. Lin, P. C. Chang, S. J. Murry, R. Q. Yang, and S. S. Pei, *Appl. Phys. Lett.* **68**, 2976 (1996).

¹⁵O. Madelung, in *Semiconductors, Group IV Elements and III-V Compounds*, edited by K.-H. Hellwege and O. Madelung, Landolt-Börnstein, New Series, Group III, Vol 17, PT. A (Springer, Berlin, 1982).

¹⁶D.-J. Jang, M. E. Flatté, C. H. Grein, J. T. Olesberg, T. C. Hasenberg, and T. F. Boggess, *Phys. Rev. B* **58**, 13047 (1998).

¹⁷J. T. Olesberg, S. A. Anson, S. W. McCahon, M. E. Flatté, T. F. Boggess, D. H. Chow, and T. C. Hasenberg, *Appl. Phys. Lett.* **72**, 229 (1998).

¹⁸S. W. McCahon, S. A. Anson, D.-J. Jang, M. E. Flatté, T. F. Boggess, D. H. Chow, T. C. Hasenberg, and C. H. Grein, *Appl. Phys. Lett.* **68**, 2135 (1996).

¹⁹S. W. McCahon, S. A. Anson, D.-J. Jang, and T. F. Boggess, *Opt. Lett.* **20**, 2309 (1995).

²⁰J. T. Olesberg, M. E. Flatté, B. J. Brown, C. H. Grein, T. C. Hasenberg, S. A. Anson, and T. F. Boggess, *Appl. Phys. Lett.* **74**, 188 (1999).

²¹W. Rideout, B. Yu, J. LaCourse, P. K. York, K. J. Beernink, and J. J. Coleman, *Appl. Phys. Lett.* **56**, 706 (1990).

²²K. Kukuchi, M. Kakui, C. E. Zah, and T. P. Lee, *IEEE Photonics Technol. Lett.* **3**, 314 (1991).

²³C. H. Henry, R. A. Logan, and K. A. Bertness, *J. Appl. Phys.* **52**, 4457 (1981); J. Manning, R. Olshansky, and C. B. Su, *IEEE J. Quantum Electron.* **19**, 1525 (1983); N. Ogasawara, R. Ito, K. Tone, and H. Nakae, *Jpn. J. Appl. Phys., Part 2* **23**, L518 (1984); K. S. Jepsen, N. Storkfelt, M. Vaa, and K. E. Stubkjaer, *IEEE J. Quantum Electron.* **30**, 635 (1994).

²⁴F. Kano, Y. Yoshikuni, M. Fukuda, and J. Yoshida, *IEEE Photonics Technol. Lett.* **3**, 877 (1991).

²⁵N. Storkfelt, B. Mikkelsen, D. S. Olesen, M. Yamaguchi, and K. E. Stubkjaer, *IEEE Photonics Technol. Lett.* **3**, 632 (1991).